

Control-structure interaction in piezoelectric deformable mirrors for adaptive optics

Kainan Wang^{1a}, David Alaluf^{2b}, Bilal Mokrani^{3c} and André Preumont^{*1}

¹Department of Control Engineering and System Analysis, Université Libre de Bruxelles (ULB),
CP. 165-55, 50 Av. F.D. Roosevelt, B-1050, Brussels, Belgium

²European Space Agency - ESA/ESTEC, Opto-Electronics Section, Keplerlaan 1, 2201 AZ Noordwijk ZH, The Netherlands

³Department of Mechanical, Materials and Aerospace Engineering, University of Liverpool,
The Quadrangle, Brownlow Hill L69 3GH, United Kingdom

(Received November 6, 2017, Revised March 4, 2018, Accepted March 8, 2018)

Abstract. This paper discusses the shape control of deformable mirrors for Adaptive Optics in the dynamic range. The phenomenon of control-structure interaction appears when the mirror becomes large, lowering the natural frequencies f_i , and the control bandwidth f_c increases to improve the performance, so that the condition $f_c \ll f_i$ is no longer satisfied. In this case, the control system tends to amplify the response of the flexible modes and the system may become unstable. The main parameters controlling the phenomenon are the frequency ratio f_c/f_i and the structural damping ζ . Robustness tests are developed which allow to evaluate a lower bound of the stability margin. Various passive and active strategies for damping augmentation are proposed and tested in simulation.

Keywords: adaptive optics; deformable mirror; control-structure interaction; active/passive damping

1. Introduction

Atmospheric turbulence produces a temporal and spatial random variation of the refraction index of the air; this is responsible for a random variation of the speed of light which distorts the wavefront of incoming plane waves (Fig. 1). Adaptive optics (AO) has revolutionized astronomy by correcting in real-time the wavefront aberrations using a deformable mirror (DM) with an array of actuators (Tyson 2000). There are AO mirrors of all sizes, but a minimum size is generally required by the field of view of the telescope; typical DM diameter for a few hundred actuators is 150-200 mm; future giant telescopes (Gilmozzi and Spyromilio 2008) will use AO mirrors with thousands of actuators and a diameter of more than one meter, e.g., the AO mirror M4 of E-ELT will have a diameter of 2.5 m and will have 5800 actuators (ESO 2011). As the size of the mirror grows, the natural frequencies of the vibration modes drop and the vibration modes tend to be excited by the control system. The interaction between the AO control system and the flexible modes of the mirror is the main subject of the present study.

The paper starts with a review of some optical background (for readers who are not familiar with Adaptive Optics); section 3 introduces briefly the various technologies for deformable mirrors, with a particular attention to the bimorph piezoelectric mirrors used later in this study. Section 4 discusses the quasi-static control using singular value decomposition; section 5 considers the feedback control based on a quasi-static model and section 6 analyzes how the closed-loop response is affected by the flexible modes, leading to control-structure interaction discussed in section 7 where criteria for avoiding the spillover instability are developed. The role of damping is highlighted and two methods for damping augmentation (passive and active) are discussed.

2. Optical background

2.1 Wavefront aberration

The wavefront aberration may be expressed either in displacement amplitude $w(r, \theta)$ (in microns) or in phase, $\phi(r, \theta) = 2\pi \cdot w(r, \theta) / \lambda$ (in radians). The root-mean-square (RMS) value over the whole optical surface is an indicator of the quality of the optical system; it is considered as nearly perfect if the RMS wavefront error is less than $\lambda/14$.

The *Fried length* r_0 defines the maximum size of a diffraction limited telescope for a given site; it is the aperture above which there is no improvement of the resolution without Adaptive Optics. If $D \leq r_0$, the telescope is diffraction limited; if $D \geq r_0$, the resolution is limited by the *seeing*: λ / r_0 ; the seeing is a property of the telescope site; it improves with altitude and depends strongly on

*Corresponding author, Professor
E-mail: andre.preumont@ulb.ac.be

^a Ph.D. Student

E-mail: kainan.wang@ulb.ac.be

^b Ph.D.

E-mail: david.alaluf@esa.int

^c Ph.D.

E-mail: bilal.mokrani@liverpool.ac.uk

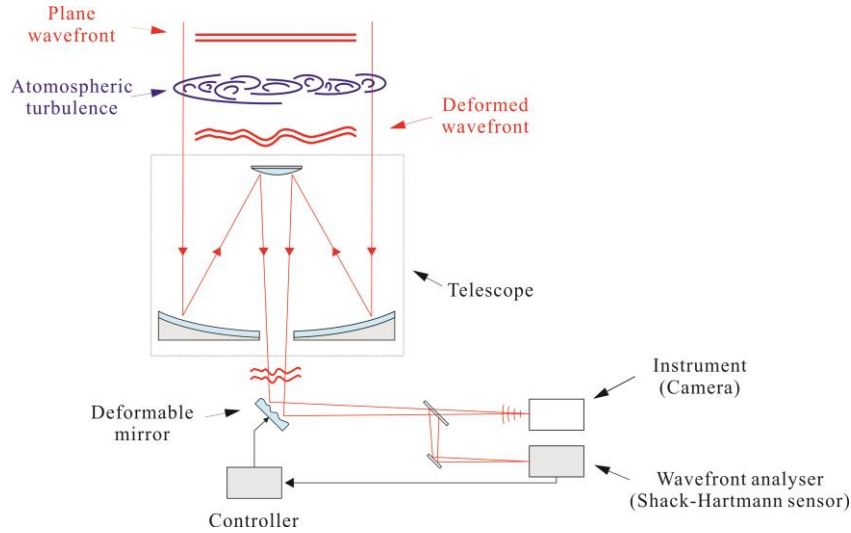


Fig. 1 Principle of adaptive optics to correct atmospheric turbulence. A small deformable mirror is controlled in real time to compensate the wavefront aberrations, measured with a wavefront sensor (Shack-Hartmann)

humidity; this is why telescopes are located in remote, mountainous and dry places such as the Atacama desert. r_0 depends on the wavelength; typical values are $r_0 = 10\text{-}20$ cm at $\lambda = 0.55 \mu\text{m}$ (visible) and $r_0 = 53\text{-}106$ cm at $\lambda = 2.2 \mu\text{m}$ (infrared).

The atmospheric turbulence may be seen as a frozen shape transported by the wind at velocity V (Taylor assumption). The phase delay associated with this frozen shape may be represented by the Kolmogorov turbulence model, (see Dainty 2000). According to this model, the Mean-Square (MS) error of the phase for a telescope of diameter D is given by

$$\sigma_\phi^2 = 1.03 \left(\frac{D}{r_0} \right)^{5/3} \quad (1)$$

If $D = r_0$, $\sigma \approx 1$ rad.

Assuming a circular pupil of radius R , the wavefront aberration is often expressed as

$$\phi(R\rho, \theta) = \sum_{i=1}^n a_i Z_i(\rho, \theta) \quad (2)$$

where $Z_i(\rho, \theta)$ are a set of orthogonal functions defined on the unit circle in polar coordinates called the *Zernike polynomials* or *Zernike modes* (Noll 1976). The analytical expressions of the low order Zernike polynomials is given in appendix.

Since the atmospheric turbulence is a random process, the MS phase error may be written

$$\sigma^2 = \sum_{i=1}^{\infty} \langle |a_i|^2 \rangle \quad (3)$$

where $\langle |a_i|^2 \rangle$ stands for the mathematical expectation of the square amplitude of the Zernike modes. The Zernike modes with low radial order have the largest contribution to the MS error.

The *Strehl Ratio* S is a measure of the image quality; it is equal to 1 for a perfect diffraction limited telescope. The so-called *Marechal Approximation* (Roddier 1999) relates S to the MS phase error by

$$S = e^{-\sigma^2} \quad (S > 0.1) \quad (4)$$

The approximation

$$S \approx 1 - \sigma^2 \quad (\sigma \ll 1) \quad (5)$$

is also often used. The threshold of image acceptability corresponds to $D = r_0$, thus $\sigma = 1$ rad, leading to $S \approx 0.37$. A well corrected system has a Strehl ratio $S \geq 0.8$, corresponding to $\sigma_\phi^2 = 0.2 \text{ rad}^2$, that is a wavefront aberration of $\sigma_w \approx \lambda/14$. Notice that the effect of a deformable mirror is to introduce a modification of the wavefront twice that of the deformed mirror within the pupil.

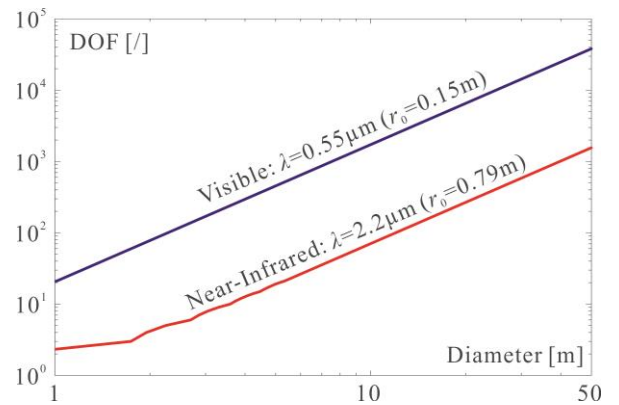


Fig. 2 Number of Zernike modes which have to be perfectly cancelled to achieve a Strehl ratio of $S = 0.5$ as a function of the diameter D of the primary mirror, for two values of the Fried length r_0

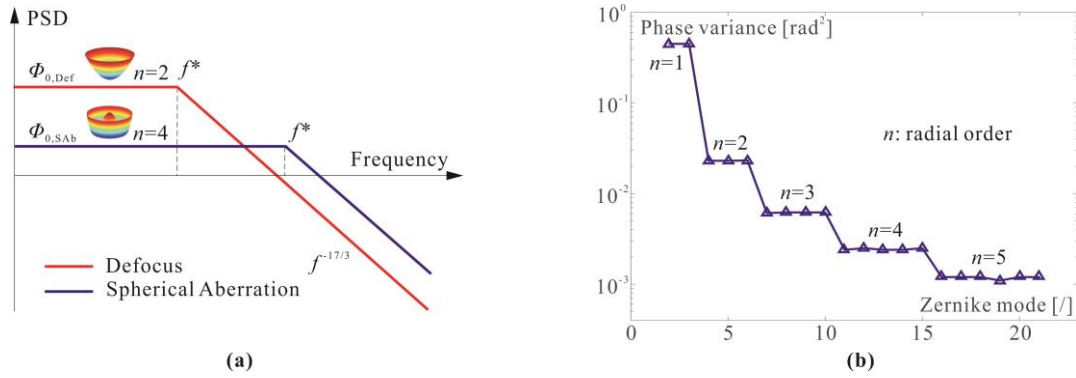


Fig. 3 (a) Sketch of the Power Spectral Density of Zernike polynomials of radial order $n = 2$ and $n = 4$; the corner frequency is $f^* = 0.3(n + 1)V/D$ and (b) Normalized phase variance of the Zernike modes: $\langle |a_i|^2 \rangle (D/r_0)^{5/3}$

Fig. 2 gives the number of Zernike modes which have to be perfectly cancelled to achieve a Strehl ratio of $S = 0.5$ as a function of the aperture D of the telescope. This number gives an indication of the number of independent actuators which will be necessary on the AO mirror; it depends strongly on the wave length. In the visible, it exceeds rapidly 1000 for diameters above 10 meters.

2.2 Power spectral density of the zernike modes

Since the atmospheric turbulence consists of a frozen random field transported by the wind, at velocity V , the Zernike mode amplitudes of the phase aberration consist of zero-mean stationary random processes. The temporal Power Spectral Density (PSD) of the amplitudes of the Zernike polynomials expansion of the phase error has been studied (Conan *et al.* 1995). For a given radial degree ($n > 1$), it can be roughly approximated by a constant value Φ_0 until the cut-off frequency f^* followed by a decay rate of $f^{-17/3}$ (Fig. 3(a)). The cut-off frequency depends on the radial order n and the wind velocity according to

$$f^* = 0.3(n+1) V/D \quad (6)$$

With this simplified model, the corresponding MS error (of Zernike polynomial of order i) without control is

$$\langle |a_i|^2 \rangle = 1.21 \Phi_0 f^* \quad (7)$$

The contribution of the various Zernike components to the total phase variance is represented in Fig. 3(b) [normalized according to $(D/r_0)^{5/3}$, so that the sum of them is equal to 1.03 as stated by Eq. (1)]. One sees that the contributions of the low order Zernike modes are significantly larger than that of the high order modes.

2.3 Wavefront sensor

Adaptive Optics requires the real-time measurement of the wavefront distortion induced by the non-uniform light propagation velocity within the telescope aperture. This is done by a beam splitter that deviates part of the incoming light towards a wavefront sensor (Fig. 1). The most popular wavefront sensor in astronomy is the *Shack-Hartmann* (S-H) sensor; it consists of an array of lenslets and a detector located at

their focal distance. If the wavefront is flat, the light coming from every lenslet converges towards the focal point of the corresponding sub-aperture; if the wavefront is tilted, the focal point will be shifted in its sub-aperture and the shift is a linear function of the slope of the wavefront. If the wavefront is curved within the sub-aperture, the light will spread in the focal plane to form a spot, but the centroid of the spot will still be a linear function of the average slope of the wavefront within the sub-aperture. Thus, a Shack-Hartmann sensor provides the measurement of the slopes of the wavefront in an array of discrete points corresponding to the various sub-apertures (each sub-aperture provides the two slopes ϕ_x and ϕ_y , with a total of sensor outputs equal to twice the number of active lenslets). Shack-Hartmann sensors are very photon-efficient and require little signal processing; they are well adapted to real time applications and the sampling frequency can reach 1000 Hz. Since the total wavefront distortion is the combination of the high frequency atmospheric turbulence and the low frequency geometric aberration of the telescope, the latter belongs to the range of *Active Optics* and can be isolated by low-pass filtering in the time domain.

3. Deformable mirrors for adaptive optics

Deformable mirrors are used in many applications, including astronomy, ophthalmology, power laser, etc.. The present discussion is limited to AO mirrors in astronomy. There are AO mirrors of all sizes, from microsystems to more than a meter, but a minimum size is generally required by the field of view of the telescope; typical DM diameter for a few hundred actuators is 150-200 mm. The number N of independent actuators (also called number of degrees of freedom - DOF) depends on the size of the telescope, the wavelength and the requested optical quality; the diagram of Fig. 2 may be regarded as a lower bound. One sees that this number may become very large for a telescope working in the visible. The most common way to actuate a deformable mirror is to apply out-of-plane forces; these forces may be generated electromagnetically by voice coils acting on tiny permanent magnets, by piezoelectric stacks, or by electrostatic actuators. An excellent review of the various technologies is available (Madec 2012). The up-scaling of these designs will inevitably increase the weight of the AO mirror and

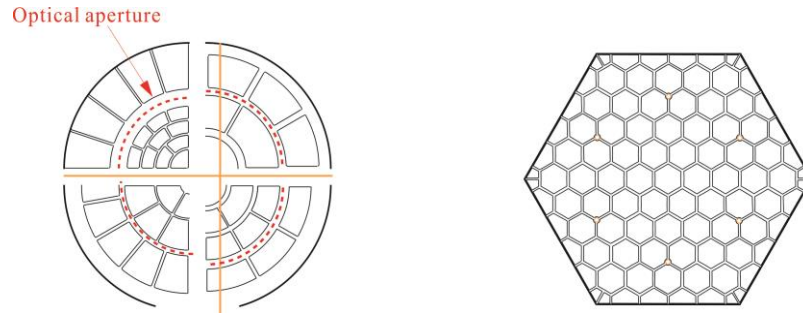


Fig. 4 Most common electrode layouts of bimorph mirrors. Left: The Keystone layout is well suited to controlling the low order Zernike modes. Right: The honeycomb layout is homogeneous and well suited to scaling up and segmented design



Fig. 5 Deformable mirror made of a 150 mm Silicon wafer covered on its back side with an array of screen printed PZT actuators with honeycomb electrodes acting in the d_{31} mode

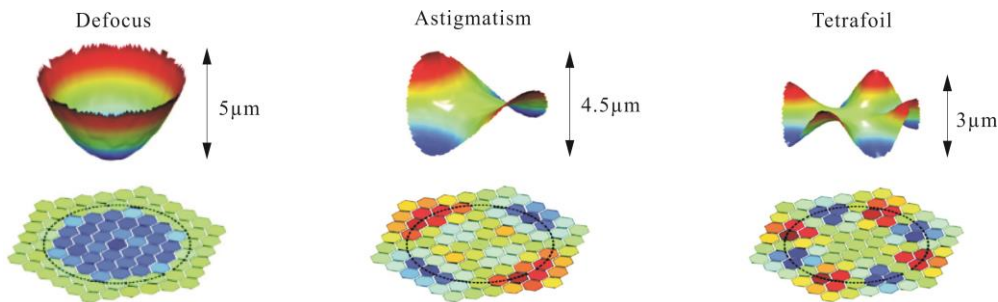


Fig. 6 Deformable mirror: typical corrected aberrations with the corresponding voltage distribution within the honeycomb electrodes (Rodrigues 2010)

the dynamic coupling with the telescope structure. Alternatively, the AO mirror can be actuated by in-plane forces generated by piezoelectric layers acting in the d_{31} -mode. These *Bimorph* mirrors have a very simple configuration, they are lightweight and can be easily produced at a relatively low cost (Gebhardt *et al.* 2007).

Fig. 4 shows the most common electrode layouts of bimorph mirrors. Fig. 5 shows a bimorph deformable mirror made of a Silicon wafer of 150 mm diameter and 800 μm thickness, covered with a thick film of PZT of 70 μm (Rodrigues *et al.* 2009); it is actuated by an array of 91 independent electrodes with a honeycomb configuration, the voltage of which can be adjusted independently between 0 and 160 V. Fig. 6 shows examples of shapes obtained experimentally with this mirror; color maps of the voltage distributions are also shown (Rodrigues 2010).

4. Quasi-static control

Once the number and shape of the actuators and the configuration of the Shack-Hartmann sensor have been chosen, the quasi-static behavior of the AO mirror is described by the linear equation

$$\mathbf{s} = \mathbf{J}\mathbf{v} \quad (8)$$

where \mathbf{s} is the vector of output of the SH sensor and \mathbf{v} is the vector of input voltages applied to the piezoelectric actuators. The actuator input which cancels the sensor output is obtained using the pseudo inverse of the Jacobian matrix

$$\mathbf{v} = \mathbf{J}^\dagger \mathbf{s} \quad (9)$$

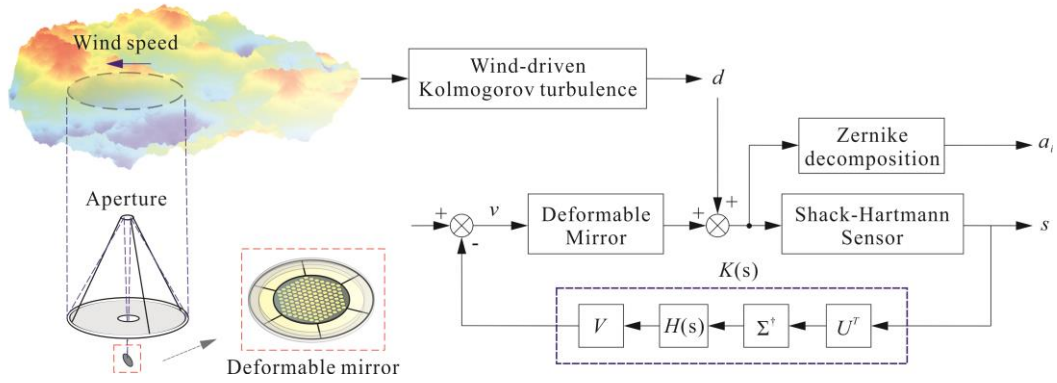


Fig. 7 Block diagram of the control system. The input-output relationship is $\mathbf{s} = \mathbf{J}\mathbf{v}$. The feedback loop consists of the SVD controller $K(s) = \mathbf{V}\mathbf{H}(s)\mathbf{\Sigma}^\dagger\mathbf{U}^T$. The disturbance d consists of a frozen Kolmogorov turbulent screen transported by the wind. The performance is measured by the Zernike expansion of the residual error

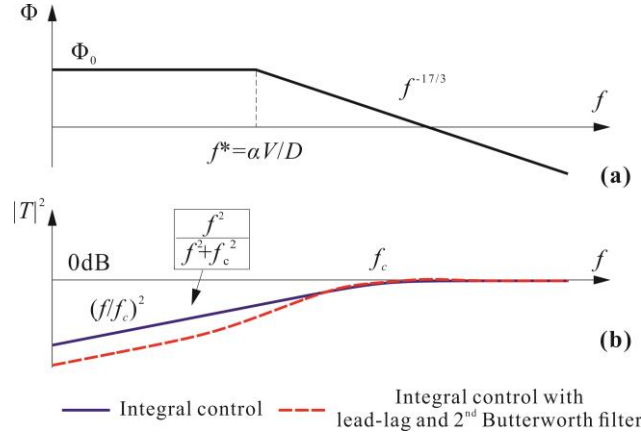


Fig. 8 (a) PSD of a Zernike polynomial; $f^* = 0.3(n+1)V/D$ where n is the radial order and (b) Squared amplitude $|T|^2$ of the sensitivity function (the compensator of Fig. 9 is in dashed lines)

If a Singular Value Decomposition (SVD) of J is carried out

$$J = \mathbf{U}\mathbf{\Sigma}\mathbf{V}^T = \sum_{i=1}^n \sigma_i \mathbf{u}_i \mathbf{v}_i^T \quad (10)$$

(\mathbf{u}_i are the orthogonal sensor modes and \mathbf{v}_i the orthogonal actuator modes), the pseudo-inverse reads

$$J^\dagger = \mathbf{V}\mathbf{\Sigma}^\dagger\mathbf{U}^T = \sum_{i=1}^n \frac{1}{\sigma_i} \mathbf{v}_i \mathbf{u}_i^T \quad (11)$$

This solution is that minimizing $\|\mathbf{s} - \mathbf{J}\mathbf{v}\|^2$. The sum normally extends to all singular values. However, because they appear as σ_i^{-1} the smallest singular values tend to generate unnecessary large control inputs without bringing any contribution to improvement of the fitting error. The problem may be solved either by truncating the SVD expansion of J^\dagger after r terms, to eliminate the smallest singular values, or to use a *Tikhonov regularization*, minimizing

$$\min[\|\mathbf{s} - \mathbf{J}\mathbf{v}\|^2 + \alpha^2 \|\mathbf{v}\|^2] \quad (12)$$

where α^2 is a tuning parameter, the method is also known as damped least squares (see Buss 2004). The solution is

$$\mathbf{v} = (\mathbf{J}^T \mathbf{J} + \alpha^2 \mathbf{I})^{-1} \mathbf{J}^T \mathbf{s} \quad (13)$$

The singular value expansion of J^\dagger now reads

$$J^\dagger = \mathbf{V}\mathbf{\Sigma}^\dagger\mathbf{U}^T = \sum_{i=1}^n \frac{\sigma_i}{\sigma_i^2 + \alpha^2} \mathbf{v}_i \mathbf{u}_i^T \quad (14)$$

5. Feedback control based on quasi-static model

5.1 SVD controller

In this approach, the mirror is assumed to behave in a quasi-static manner and the wavefront is measured by a SH sensor; the input-output relationship between the voltages applied to the control electrodes and the SH sensor output is defined by the Jacobian J of Eq. (8). The block diagram of the control system is shown in Fig. 7. The disturbance d consists of a frozen Kolmogorov turbulent screen

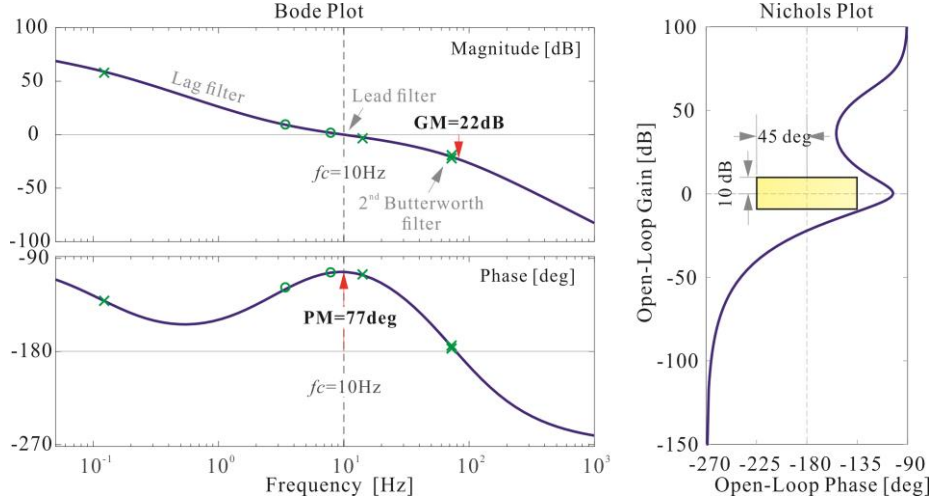


Fig. 9 Compensator with improved performance (normalized to $f_c = 10$ Hz). It consists of an integrator, a lag filter, a lead filter and a Butterworth second order filter. The position of the poles and zeros are indicated on the Bode plots (left). The bandwidth may be adjusted by translating the Bode plots along the frequency axis until the proper crossover frequency f_c is reached. This leaves the Nichols plot (right) unchanged

transported at the wind velocity. The performance is measured by the Zernike expansion of the residual phase variance.

The feedback loop consists of a SVD controller: $V\Sigma^\dagger U^T$ is the inverse of the plant (the Jacobian J). The sensor output is projected into the sensor modes U ; the diagonal pseudo inverse matrix Σ^\dagger provides an equal authority on all singular value modes; the set of filters $H(s)$ provide adequate disturbance rejection and stability margin; $H(s)$ may be a scalar function if the same loop shaping is applied to all the output modes. Finally, the commands are converted into voltages by the projection matrix V (actuator modes). We now examine the effect of the SVD controller on the Zernike modes.

5.2 Control of Zernike modes

As discussed earlier, the PSD $\Phi(f)$ of the Zernike modes may be roughly approximated as represented in Fig. 8(a). In order to analyze the residual error with feedback control, let us first assume that all the control loops use the same filter $H(f) = f_c/jf$ (integral control with crossover frequency f_c); this filter is convenient to derive simple analytical results and guarantee a zero static error; a more sophisticated one will be discussed below. The transfer function between the disturbance and the system output error is given by the sensitivity function (Fig. 8(b))

$$T = \frac{1}{1+H} = \frac{1}{1+f_c/jf} \quad |T|^2 = \frac{f^2}{f^2 + f_c^2}$$

The closed-loop MS residual error in the Zernike mode i is given by

$$\langle |a_i|^2 \rangle_{CL} = \int_0^\infty |T|^2 \Phi(f) df \quad (15)$$

where $\Phi(f)$ is the PSD of the Zernike mode. Assuming for

$\Phi(f)$ the shape of Fig. 8(a) and that $f_c \gg f^*$, one finds

$$\langle |a_i|^2 \rangle_{CL} \approx 0.708 \Phi_0 f_c^* \left(\frac{f_c^*}{f_c} \right)^2 \approx 0.585 \langle |a_i|^2 \rangle \left(\frac{f_c^*}{f_c} \right)^2 \quad (16)$$

after using Eq. (7). Thus, the ratio between the closed-loop and the open-loop variance reads

$$\frac{\langle |a_i|^2 \rangle_{CL}}{\langle |a_i|^2 \rangle} \approx 0.585 \left(\frac{f_c^*}{f_c} \right)^2 \quad (17)$$

Since f^* increases with the radial order of the Zernike mode, the foregoing result might suggest that f_c should be larger for higher order modes; however, as rightly observed by (Conan *et al.* 1995), the contribution $\langle |a_i|^2 \rangle$ of the Zernike modes with low radial orders to the total MS error is much larger than that of the higher modes (Fig. 3(b)), necessitating a higher control bandwidth for the low order modes.

The integral controller used above is convenient for illustration purposes and computing orders of magnitude, but it does not provide optimal performances and, as we shall see next, it is prone to spillover (i.e., exciting the dynamics not included in the model of the plant). In the compensator of Fig. 9, the integral control has been supplemented with a lag filter to magnify the gain at low frequency; a lead filter is included near crossover to increase the phase margin and a second order Butterworth filter is added at high frequency to increase the roll-off and reduce spillover. The poles and zeros of the compensator are shown in the figure. The controller may be scaled to the appropriate bandwidth by simply translating the Bode plots along the frequency axis until the crossover frequency f_c has the appropriate value. The square amplitude of the sensitivity function $|T|^2$ has been added in dashed lines in Fig. 8(b). The effect of this compensator on the Zernike modes can be analyzed numerically.

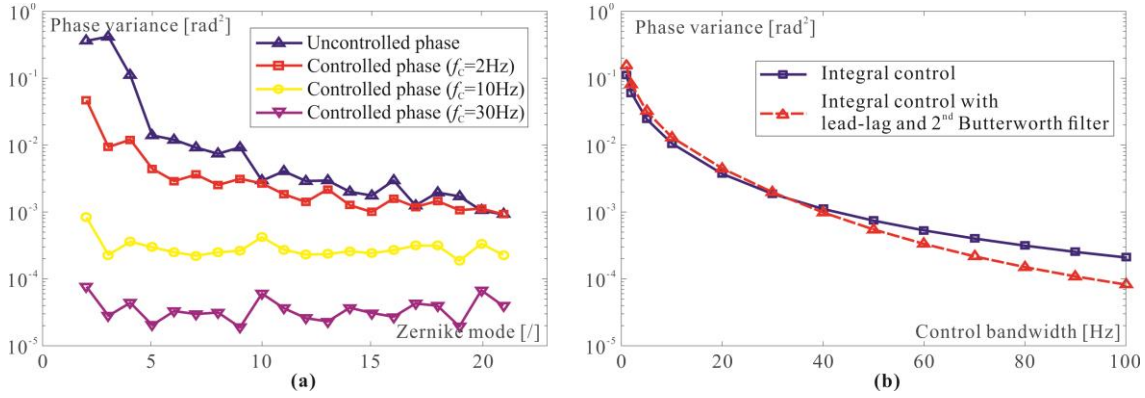


Fig. 10 Estimated closed-loop performance. (a) Normalized phase variance of the Zernike Modes $\langle |a_i|^2 \rangle (D/r_0)^{-5/3}$ for various values of the crossover frequency f_c using the controller in Fig. 9 and (b) Normalized phase variance $\sigma_{CL}^2 (D/r_0)^{-5/3}$, for various values of crossover frequency f_c .

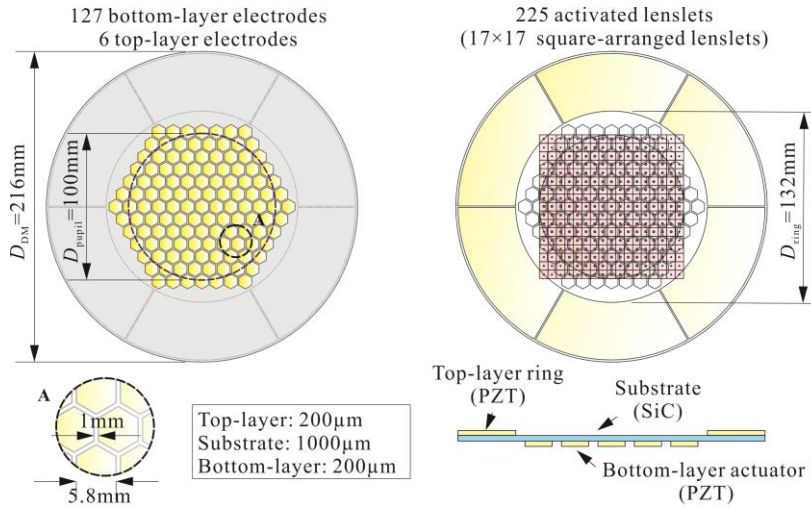


Fig. 11 AO mirror configuration used in the simulations. The left side shows the piezoelectric actuator array and the right side shows the lenslet array of the SH sensor

A simulation code has been developed (Wang *et al.* 2017) which allows to generate turbulent screens with Kolmogorov distribution (for a given Fried length r_0) and calculate the time-history of the Zernike mode amplitudes when the turbulent screen is transported by the wind at a velocity V over the telescope aperture D . From the time-histories, the PSD are estimated. The closed-loop MS amplitude is then calculated using Eq. (15). The following data have been assumed in the calculations: telescope aperture: $D = 5$ m, Fried coherence length: $r_0 = 79$ cm (defined at $\lambda = 2.2 \mu\text{m}$ for a 0.57 arcsec seeing), wind speed $V = 10$ m/s. Fig. 10(a) shows the evolution of the normalized phase variance amplitude of the Zernike modes for various values of the crossover frequency f_c of the integral controller; Fig. 10(b) shows the normalized cumulative phase variance with the two controllers as a function of f_c ; it is based on the first 100 Zernike modes

$$\left\{ \sum_{i=2}^{100} \langle |a_i|^2 \rangle_{CL} \right\} (D/r_0)^{-5/3}$$

The residual phase variance may be transformed directly in optical quality using Eq. (4). Recall that all the foregoing results have been obtained assuming a quasi-static behavior of the mirror; the influence of the flexible modes is analyzed below.

6. Dynamic response of the AO mirror

6.1 Dynamic model of the mirror

The simulation has been extended to include a dynamic model of the mirror, a representation of the piezoelectric effects (Piefort 2001) (Marinkovic 2012), and a model of the Shack-Hartmann (SH) sensor (assuming perfect dynamics). The mirror used in the simulation is represented in Fig. 11; it consists of a SiC substrate of 216 mm diameter and 1000 μ m thickness, covered on its back by an array of 127 PZT actuators of 200 μ m with honeycomb electrodes. The pupil has a diameter of 100 mm and the SH sensor consists of a square array of 17 \times 17 lenslets (225 activated).

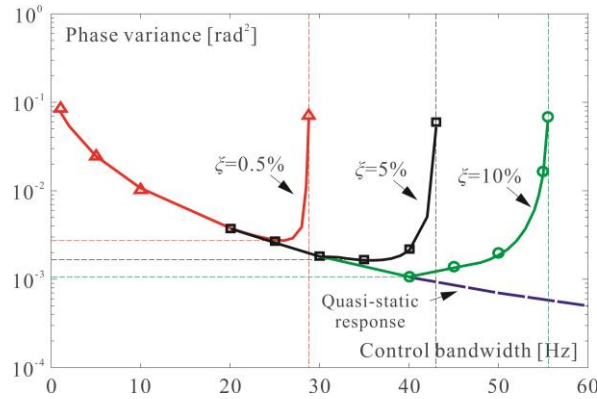


Fig. 12 Phase variance residual error when the SH and the dynamics of the mirror are included in the analysis as a function of the crossover frequency f_c of the controller of Fig. 9. The deterioration of the performance for larger f_c is highly dependent on the damping ξ

The front side of the mirror is supplemented by a ring of piezoelectric material outside the pupil, whose double role is to improve the thermal balance and provide additional damping to the system (this will be clarified later). It is assumed that a separate mirror takes care of the tip-tilt disturbance, so that the control system discussed here handles the Zernike modes of radial order $n \geq 2$. Several boundary conditions are possible, which affect the Jacobian as well as the spectrum of natural frequencies of the mirror; in this study, the mirror is assumed simply supported on the edge, but there is no restriction to applying other boundary conditions.

If K_a stands for the matrix relating the input voltages to the equivalent piezoelectric forces acting on the mirror, Φ is the matrix of mode shapes (normalized to a unit modal mass) and S is the matrix relating the SH output to the deflections of the mirror, the mirror input-output matrix may be written

$$G(s) = S\Phi \cdot \text{diag} \left[\frac{1}{s^2 + 2\xi_i \omega_i s + \omega_i^2} \right] \Phi^T K_a \quad (18)$$

where ω_i are the resonance frequencies and ξ_i the modal damping of the various vibration modes. The size of $G(s)$ is (450×127) in this case. With these notations, the Jacobian describing the quasi-static response of the mirror reads

$$J = G(0) = S\Phi \cdot \text{diag} \left[\frac{1}{\omega_i^2} \right] \cdot \Phi^T K_a \quad (19)$$

It is clear that the control approach based on a quasi-static model is legitimate if the crossover frequency of the compensator is very small compared to the natural frequencies of the AO mirror: $f_c \ll f_i = \omega_i / 2\pi$. However, as the AO mirrors become larger and the control bandwidth increases, this condition is no longer satisfied and the dynamic response of the mirror will interfere with the control system, leading to spillover and eventually to *spillover instability* (Balas 1978) (Preumont 2018).

6.2 Residual phase variance error

We now re-examine the residual phase variance error

when the dynamic response of the mirror is accounted for. Referring to Fig. 7, the simulation includes a dynamic model of the deformable mirror while the controller is based on a quasi-static model of the mirror (SVD controller). Fig. 12 shows the phase variance residual error of the mirror, for various values of the modal damping, when the time-history analysis includes the SH sensor and a dynamic model of the mirror; the compensator is that of Fig. 9. The phase variance corresponding to a quasi-static response is shown in dashed lines. For low values of the crossover frequency f_c , the results of the dynamic and the quasi-static analyses are identical, but when f_c increases, the dynamic response of the mirror tends to deteriorate the phase error because of the contribution of the flexible modes of the mirror; for larger values of f_c , the system becomes unstable. One sees that the phase error deterioration occurs even though the control bandwidth f_c is much below the first resonance of the mirror ($f_1 = 208.9$ Hz in this case), and that it depends strongly on the structural damping of the mirror. This phenomenon is known as *control-structure interaction*; it is explained below.

7. Control-structure interaction

7.1 SISO system

To introduce the problem, let us first consider the SISO position control system of Fig. 13; it consists of a single axis piezoelectric actuator of stiffness k_a acting on a mass m (representing the mirror). If δ is the unconstrained piezoelectric displacement (proportional to the voltage applied), the actuator may be modelled as a spring of stiffness k_a in parallel with a force actuator $k_a \delta$ (see Preumont 2018). It is straightforward to establish that the input-output relationship of the system is

$$x/\delta = G(f) = \frac{1}{1 + 2j\xi f/f_n - (f/f_n)^2} \quad (20)$$

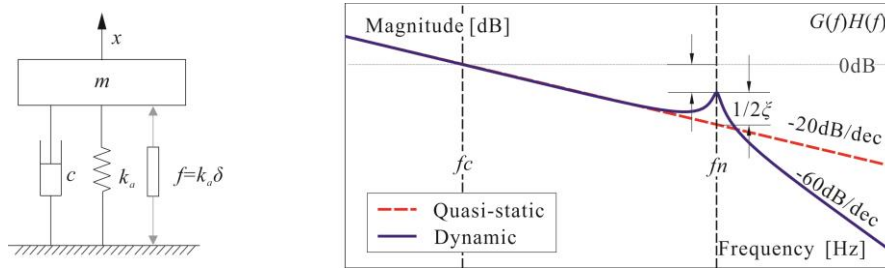


Fig. 13 Left: Position control of a single axis system with a piezoelectric actuator of stiffness k_a and unconstrained piezoelectric displacement δ . Right: Bode amplitude plot of the open-loop FRF $G(f)H(f)$

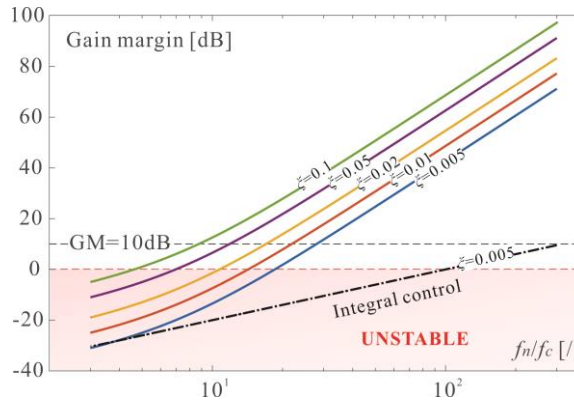


Fig. 14 SISO system of Fig. 13 controlled with the compensator of Fig. 9. Gain margin in dB as a function of the frequency ratio f_n/f_c for various values of the structural damping ξ

with $f_n = \omega_n/2\pi$, $\omega_n^2 = k_a/m$ and $2\xi\omega_n = c/m$. The compensator is the integral control $H(f) = f_c / jf$ as previously. If the structure is assumed to behave quasi-statically, $G(f) = 1$ and $G(f)H(f) = f_c / jf$ which has infinite gain margin (GM) and 90° phase margin (PM). On the contrary, if the full dynamics is included, the amplitude Bode plot of the control system is that on the right side of Fig. 13. Accordingly, the system stability requires that $f_n/f_c > 1/2\xi$ and the gain margin is expressed simply as

$$GM = 20 \log \left[\frac{2\xi f_n}{f_c} \right] \quad (\text{in dB}) \quad (21)$$

This formula points out the two parameters which dominate the control-structure interaction: the frequency ratio f_n/f_c and the structural damping ξ . Of course, the compensator used in this analysis is not the best possible one, and the situation may be improved by adding a Butterworth filter as the one of Fig. 9, but for a given compensator, the two parameters remain the same. Fig. 14 gives the gain margin (in dB) as a function of the frequency ratio f_n/f_c for a few values of the damping ratio ξ , for the compensator of Fig. 9. Eq. (21) is represented in dashed line. The interest of increasing the damping of the structure is obvious from this plot. The damping augmentation can be done passively or actively.

7.2 MIMO system

For the Multi-Input Multi-Output (MIMO) system

governed by Eq.(18), the problem is more complex, but one can use the stability robustness tests based on the small gain theorem to develop a *sufficient* condition for stability (Doyle and Stein 1981) (Maciejowski 1989) (Kosut *et al.* 1983): Accordingly, the dynamic system $G(s)$ may be decomposed into its nominal (quasi-static) part $G_0 = J$ and the residual one $G_R(s)$

$$G_R(s) = G(s) - G_0 = S\Phi \cdot \text{diag} \left[\frac{1}{s^2 + 2\xi_i \omega_i s + \omega_i^2} - \frac{1}{\omega_i^2} \right] \cdot \Phi^T K_a \quad (22)$$

In this way, the control structure interaction problem can be easily transformed into a classical form of multiplicative uncertainty (Fig. 15) for which the following sufficient condition for stability applies

$$\bar{\sigma}(G_0^{-1} G_R) < \underline{\sigma}[I + (K G_0)^{-1}] \quad (23)$$

where $\bar{\sigma}$ and $\underline{\sigma}$ stand respectively for the maximum and the minimum singular value and $K(s)$ is the SVD controller inverting the plant (Fig. 7); the inverse G_0^{-1} must be understood as a pseudo-inverse. The left hand side expresses the relative value of the residual response (G_R) with respect to the quasi-static one (G_0); it is small at low frequency and becomes large in the vicinity of the vibration modes, where the amplitude of the peaks is governed by the structural damping; increasing the structural damping will lower the resonance peaks and increasing the natural frequencies of the structure will move them to the right. The right hand side of Eq. (23) is concerned only with the nominal system; the curve is essentially flat within the

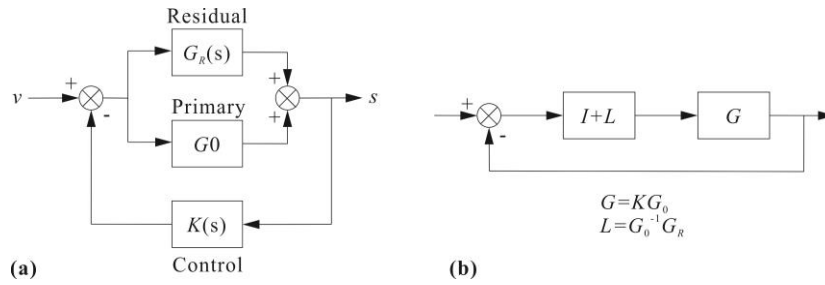


Fig. 15 (a) Block diagram of the control system with the residual dynamics and (b) Multiplicative uncertainty

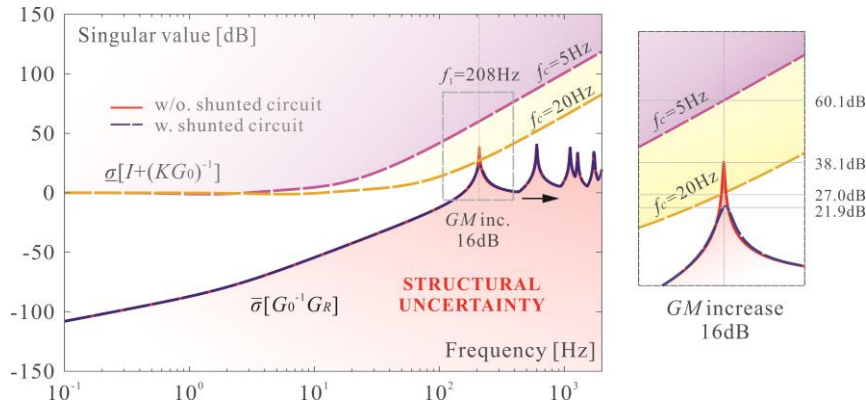


Fig. 16 MIMO stability robustness test for various values of f_c . A structural damping of 0.5% is assumed. The effect of inductive shunt damping of the first mode of vibration is shown on the structural uncertainty curve (a zoom of the first resonance is shown on the right side)

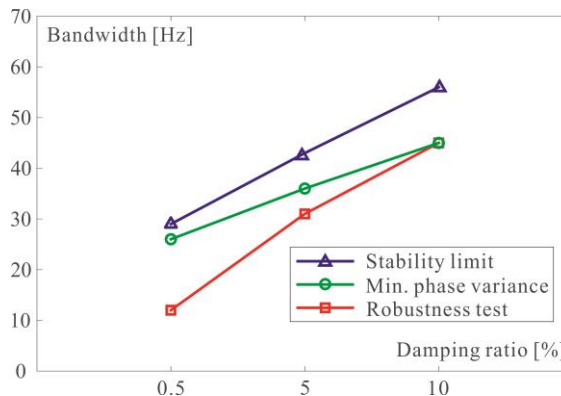


Fig. 17 Maximum crossover frequency f_c as a function of the structural damping. The lower curve is that predicted by the robustness test, the upper one is the stability limit predicted by the time-history analysis and the middle one is that corresponding to the minimum variance in Fig. 12

bandwidth of the control system; above the crossover frequency, the rate of increase is the inverse of the roll-off rate of KG_0 . Fig. 16 shows the result of the application of this test to our problem; a structural damping of 0.5% has been assumed; the distance between the two curves may be interpreted as a lower bound of the gain margin; if the two curves cross each other, there is a danger of instability. One sees that for a control bandwidth of $f_c = 20$ Hz, the stability robustness test is violated; this can be alleviated by increasing the modal damping of the first vibration mode of the mirror as discussed below.

The degree of conservatism of the robustness test may be estimated from Fig. 17 which compares the prediction of the robustness test to the stability limit predicted by the time-history analysis. The value of f_c corresponding to the minimum variance in Fig. 12 is also indicated (above this value, the phase variance begins to deteriorate).

7.3 How to handle the mirror dynamics?

The first option coming to mind is to use the “brute force” and to develop a model-based dynamic controller,

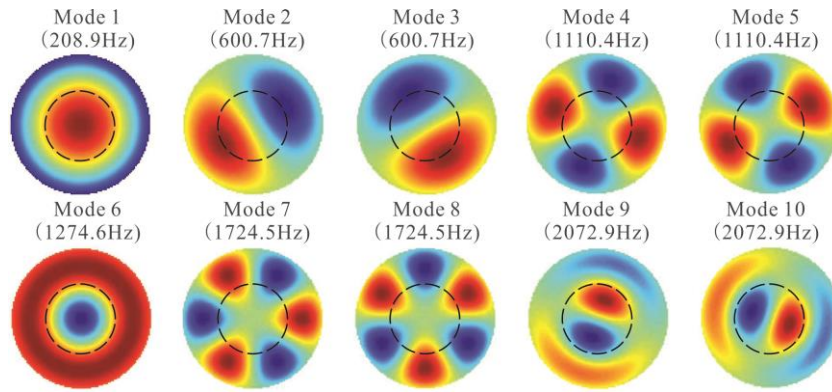


Fig. 18 Vibration mode shapes and natural frequencies of the AO mirror of Fig. 11. The pupil is represented in dashed lines. Notice the possible confusion between mode 1 and mode 6 within the pupil, and similarly between modes 2-3 and 9-10

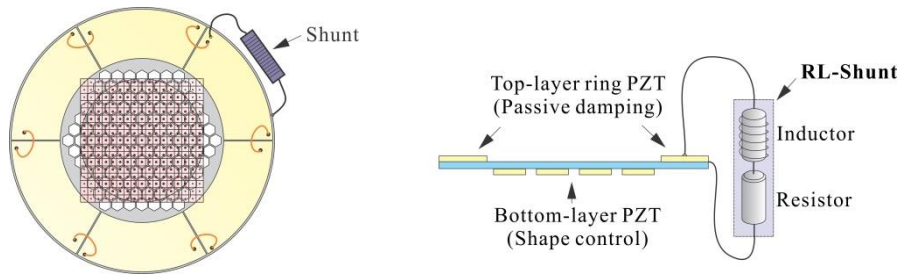


Fig. 19 Passive damping with RL shunt of the front layer ring of PZT

using for example a LQG technique, see e.g., (Nechak *et al.* 2014) (Kulcsar *et al.* 2012). This approach brings difficulties: (i) the flexible modes have rather high frequencies (see Fig. 18), leading to tough constraints on the sampling frequency, and (ii) the modal density increases rapidly with the order of the modes; how many of them should be included (where to truncate the model)? What about spillover of the higher modes?

On the other hand, we have seen in the previous section that the dynamic behavior of the mirror remains very close to the quasi-static one, even for large values of the control bandwidth, provided that the structural damping is large enough. Based on this observation, the damping augmentation (passive or active) has been selected to handle the mirror dynamics. It is discussed below.

7.4 Passive damping

The vibration modes retained in the reduced-order numerical model are represented in Fig. 18, which assumes that the first 10 modes dominate the dynamics of the system. In the configuration represented in Fig. 11, the front side of the mirror is equipped with a ring of piezoelectric material; the electrode is segmented in 6 parts, which offers the possibility to combine them in different ways, depending on the targeted mode. In this case, the first mode is axisymmetric, so that the six segments have the same curvature; it is therefore possible to connect the six piezoelectric patches in parallel to a single RL circuit

(Hagood and von Flotow 1991), which is illustrated in Fig. 19. With adequate tuning of the inductive shunt, it is possible to achieve $\zeta_1 = 0.053$ which reduces significantly the resonance peak as shown in Fig. 15. The passive damping can be further enhanced using a negative capacitance (de Marneffe 2007). Note that, beyond the damping discussed here, the PZT patches on the front side improve the thermal balance of the mirror. Besides, the outer ring may be used to introduce a concave curvature, which allows to apply control voltages at the back of the mirror with a positive bias (Alaluf 2016).

7.5 Active damping

Another option consists of implementing a low authority active control loop (LAC) using the same sensor and actuator array pairs (Fig. 20), which takes advantage of the large sensor array (SH) and the large PZT actuator array to implement modal filters. Modal active damping is applied to the critical modes which threaten the stability of the shape control loop. Modal filters were pioneered in (Meirovitch and Baruh 1985). Large sensor arrays are commonly used in vibration-based health monitoring, see e.g., (Deraemaeker *et al.* 2010) (Mendrok and Uhl 2010) (Mendrok *et al.*, 2015). In the present study, instead of designing a specific transducer array for vibration control (Zenz *et al.* 2013) and spillover reduction (Cinquemani *et al.* 2015), the active damping loop uses the PZT actuator array and SH sensor array already used for the shape control of the mirror, without any addition.

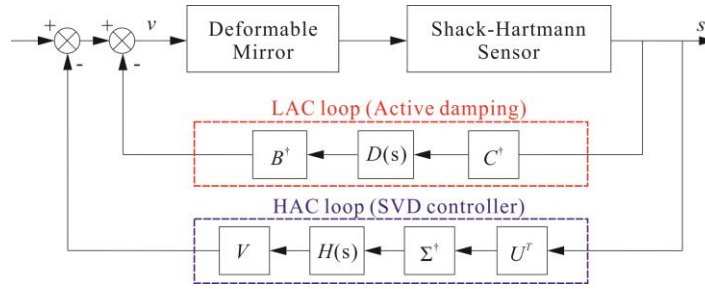


Fig. 20 HAC/LAC strategy for active damping of the mirror. The shape control loop (HAC) is supplemented by a modal active damping (LAC) of the critical low frequency modes

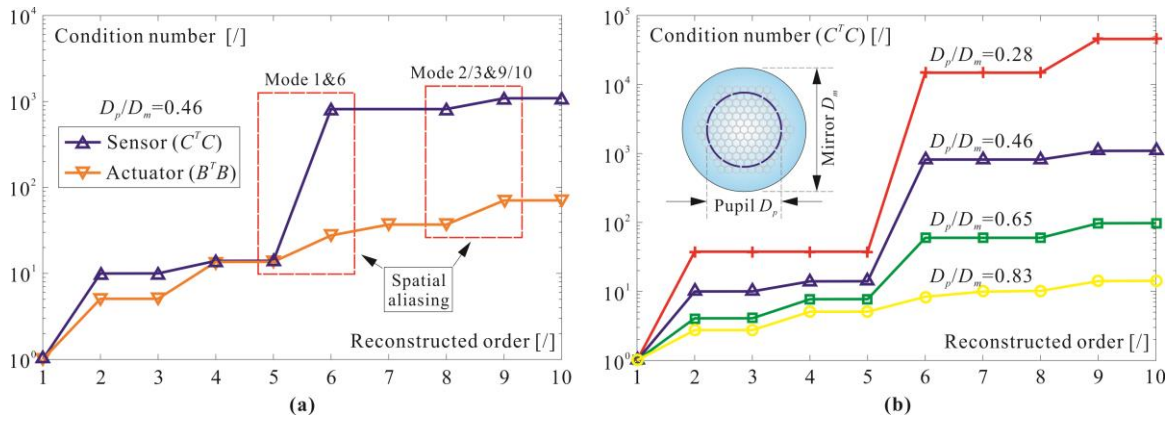


Fig. 21 (a) The condition number of $C^T C$ and $B^T B$ as a function of reconstructed orders and (b) The condition number of $C^T C$ as a function of reconstructed orders with various pupil diameters

The starting point is Eq. (18). If $\hat{\Phi}$ is the set of modes that must be reconstructed (a small number of low frequency modes), the matrices $C = S\hat{\Phi}$ and $B = \hat{\Phi}^T K_a$ may be constructed and the pseudo-inverse C^\dagger and B^\dagger may be computed (taking care of possible ill-conditioning as discussed before). If \mathbf{s} is the output vector of the SH sensor, the modal amplitudes of the reconstructed modes read

$$\hat{\mathbf{z}} = C^\dagger \mathbf{s} = (S\hat{\Phi})^\dagger \mathbf{s} \quad (24)$$

Next, a set of damping filters may be introduced to provide the selected modes with the appropriate active damping ζ_i^d

$$D(s) = \text{diag}(2\zeta_i^d \omega_i s) \quad (25)$$

Finally, the modal control is projected on the control electrodes by the matrix B^\dagger

$$\mathbf{v} = B^\dagger D(s) C^\dagger \mathbf{s} \quad (26)$$

Spatial aliasing: Although orthogonal over the entire mirror, the vibration modes are not orthogonal within the limited size of the pupil, which leads to some ill conditioning in the C and B matrices as illustrated in Fig. 21. Fig. 21(a) shows the condition number of the matrices $C^T C$ and $B^T B$ as a function of the reconstruction order; one sees that the condition number increases sharply when an ambiguous mode is added to the reconstructed ones. Observe that the matrix B is better conditioned than C

because the actuator array extends beyond the pupil of the mirror. Fig. 21(b) indicates that the ill-conditioning of C depends very much on the size of the pupil. This is responsible for spatial aliasing in the modal filter, as illustrated in Fig. 22 that represents the modal input-output relationship for mode 1 and mode 2 and 3 respectively. Fig. 22(b) shows the ideal modal filter for mode 1 and the actual one when mode 6 (which has a shape similar to mode 1 inside the pupil) is included or excluded of the matrix C . One sees that if mode 6 is included in the $\hat{\Phi}$ matrix, the modal filter follows nicely the ideal one, while in the other case, a spurious peak appears in the modal filter at the frequency $f_6 = 1274.6$ Hz of the ambiguous mode. The same phenomenon is observed in Fig. 22(c) for modes 2-3 and modes 9-10. Note that, if the sampling rate of the control loop is limited, the spurious component in the modal filter will be aliased in the time domain and appear at a lower frequency, which will degrade the closed-loop performance of the AO system.

To illustrate this, Table 1 shows the results of time domain simulations performed with a dynamic model of the mirror and the controller of Fig. 9; a modal damping of 0.5% is assumed for the vibration modes. Two values of the control bandwidth are considered, $f_c = 20$ Hz for which the dynamic model follows closely the quasi-static one, and $f_c = 30$ Hz which is unstable (Fig. 12); two values of the sampling frequency are considered, $f_s = 1000$ Hz and $f_s = 2000$ Hz.

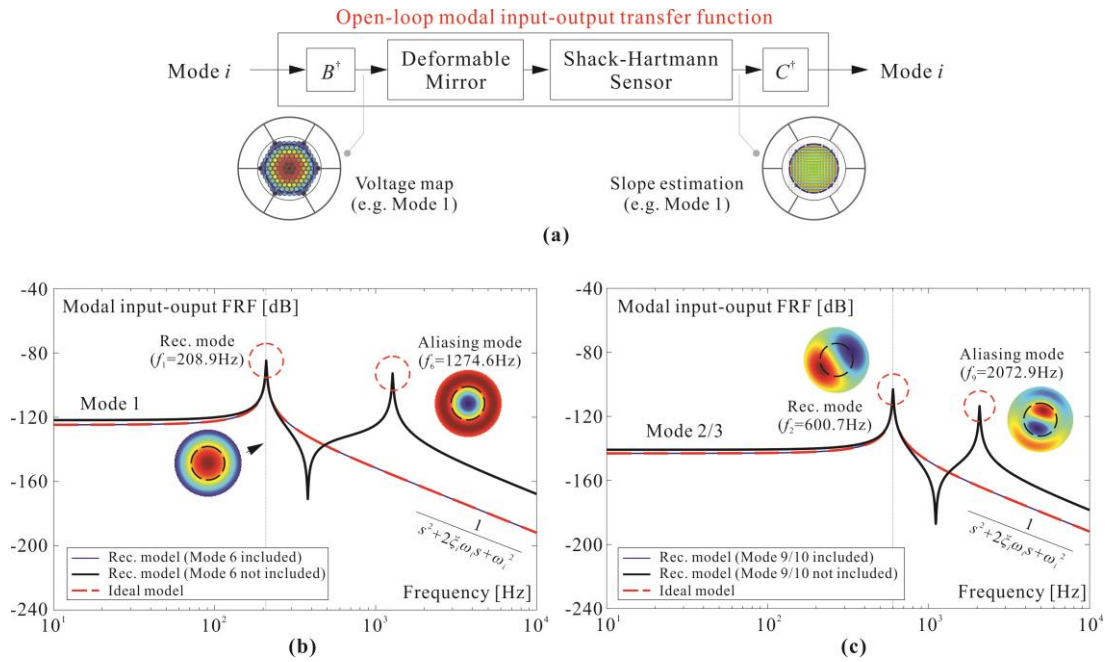


Fig. 22 (a) Block diagram of the open-loop modal input-output relationship. Modal filter: comparison between the ideal filter and the reconstructed model, (b) Mode 1 and (c) Modes 2 and 3

Table 1 Time-history calculation of the closed-loop system with HAC/LAC strategy

Reconstructed modes	Corrected modes	Phase variance [$\times 10^{-3} / (D/r_0)^{5/3}$]	
		$f_s = 1000$ Hz	$f_s = 2000$ Hz
$f_c = 20$ Hz			
	Quasi-static model	3.95	3.74
	LAC loop deactivated	4.00	3.79
	1-6	3.95	3.75
	1-6	7.19 ^(†,*)	5.04 ^(†)
	1-10	3.96 ^(*)	3.75
$f_c = 30$ Hz			
	Quasi-static model	1.96	1.81
	LAC loop deactivated	UNSTABLE	
	1-6	2.05	1.91
	1-6	5.23 ^(†,*)	3.13 ^(†)
	1-10	2.06 ^(*)	1.91

^(†) Spatial aliasing.

^(*) Temporal aliasing.

The quasi-static model is taken as reference. In the first set of results, one sees that if the LAC loop of the controller is deactivated (quasi-static control), there is a small penalty due to the vibration of the mirror; the penalty disappears if the LAC loop is activated on mode 1 and the reconstruction includes modes 1 to 6 (to include the ambiguous mode). However, the response is degraded if one wants to control mode 1 to 3 in the LAC loop without reconstructing the ambiguous modes 9 and 10 (because of spatial and temporal aliasing). The penalty disappears if modes 1 to 10 are included in the reconstruction; a very small degradation (3.96 instead of 3.95) is observed when $f_s = 1000$ Hz because of temporal aliasing of mode 2 ($f_2 = 600.7$ Hz is

aliased into a component at 499.3 Hz). For $f_c = 30$ Hz, the control system is unstable when the LAC loop is deactivated and one can recover nearly the performance of a quasi-static model when the LAC loop is activated with active damping of mode 1. The previous observations regarding the mode reconstruction may be repeated here.

8. Conclusions

Large deformable mirrors are often necessary to accommodate a large number of actuators; this usually results in a low natural frequency f_1 which conflicts with the control bandwidth, leading to control-structure interaction and possibly spillover instability. The main parameters controlling the phenomenon are the frequency ratio f_c / f_1 and the structural damping ζ . Robustness tests have been used which allow to evaluate a lower bound of the stability margin. Various ways of damping augmentation (passive and active) have been explored and it has been shown that, by increasing the damping of very few low frequency vibration modes of the mirror, it is possible to increase significantly the bandwidth of the AO control system.

An alternative way to solve the problem associated with the low values of the resonance frequencies is to use a segmented AO mirror (Bastaitis *et al.* 2014) for which the natural frequency f_1 is that of a segment, no matter how many segments form the mirror and thus, the resonance frequency is independent of the size of the AO mirror. However, segmented AO mirrors cannot operate with a SH wavefront sensor alone, because the SH sensor cannot detect the piston motion; it must be complemented by *edge sensors* which measure the relative displacement between adjacent segments.

Acknowledgments

The authors gratefully acknowledge the support from the China Scholarship Council (Grant No. 201406250021), the European Space Agency (GSTP Project BIALOM & MATS) and the Walloon Region.

References

- Alaluf, D. (2016), "Piezoelectric mirrors for adaptive optics in space telescopes", Ph.D. dissertation, Université Libre de Bruxelles, Brussels, Belgium.
- Balas, M.J. (1978), "Active control of flexible systems", *J. Optimiz. Theory Appl.*, **25**(3) 415-436.
- Bastaits, R., Alaluf, D., Belloni, E., Rodrigues, G. and Preumont, A. (2014), "Segmented bimorph mirrors for adaptive optics: morphing strategy", *Appl. Optics*, **53**(22) 4825-4832.
- Buss, S.R. (2004), "Introduction to inverse kinematics with jacobian transpose, pseudoinverse and damped least squares methods", *IEEE Robot. Autom.*, **17**(1-19) 16.
- Cinquemani, S., Ferrari, D. and Bayati, I. (2015), "Reduction of spillover effects on independent modal space control through optimal placement of sensors and actuators", *Smart Mater. Struct.*, **24**(8) 085006.
- Conan, J. M., Rousset, G. and Madec, P. Y. (1995), "Wave-front temporal spectra in high-resolution imaging through turbulence", *J. Opt. Soc. Am. A*, **12**(7) 1559-1570.
- Dainty, J.C. (2000), "Optical effects of atmospheric turbulence", in *Laser Guide Star Adaptive Optics for Astronomy*, Springer Netherlands, Dordrecht, Netherlands.
- de Marneffe, B. (2007), "Active and passive vibration isolation and damping via shunted transducers", Ph.D. dissertation, Université Libre de Bruxelles, Brussels, Belgium.
- Deraemaeker, A., Preumont, A., Reynders, E., De Roeck, G., Kullaa, J., Lamsa, V., Worden, K., Manson, G., Barthorpe, R., Papatheou, E. and Kudela, P. (2010), "Vibration-based structural health monitoring using large sensor networks", *Smart Struct. Syst.*, **6**(3) 335-347.
- Doyle, J.C. and Stein, G. (1981), "Multivariable feedback design: concepts for a classical/modern synthesis", *IEEE Robot. Autom.*, **26**(1) 4-16.
- European Southern Observatory (2011), *The E-ELT construction proposal*, ESO, Garching bei München, Germany.
- Gebhardt, S., Seffner, L., Schlenkrich, F. and Schönecker, A. (2007), "PZT thick films for sensor and actuator applications", *J. European Ceramic Society*, **27**(13) 4177-4180.
- Gilmozzi, R. and Spyromilio, J. (2008), "The 42 m European ELT: status", *SPIE Astronomical Telescopes + Instrumentation*, Marseille, July.
- Hagood, N.W. and von Flotow, A. (1991), "Damping of structural vibrations with piezoelectric materials and passive electrical networks", *J. Sound Vib.*, **146**(2) 243-268.
- Hansen, P.C. and O'Leary, D.P. (1993), "The use of the L-curve in the regularization of discrete ill-posed problems", *SIAM J. Sci. Comput.*, **14**(6) 1487-1503.
- Kosut, R.L., Salzwedel, H. and Emami-Naeini, A. (1983), "Robust control of flexible spacecraft", *AIAA J. Guid. Control Dynam.*, **6**(2) 104-111.
- Kulcsár, C., Raynaud, H.F., Petit, C. and Conan, J.M. (2012), "Minimum variance prediction and control for adaptive optics", *Automatica*, **48**(9) 1939-1954.
- Maciejowski, J.M. (1989), *Multivariable feedback design*, Addison-Wesley, Wokingham, Berkshire, UK.
- Madec, P.Y. (2012), "Overview of deformable mirror technologies for adaptive optics and astronomy", *SPIE Astronomical Telescopes + Instrumentation*, Amsterdam, September.
- Marinkovic, D. and Marinkovic, Z. (2012), "On FEM modeling of piezoelectric actuators and sensors for thin-walled structures", *Smart Struct. Syst.*, **9**(5) 411-426.
- Meirovitch, L. and Baruh, H. (1985), "The implementation of modal filters for control of structures", *AIAA J. Guid. Control, Dynam.*, **8**(6) 707-716.
- Mendrok, K. and Uhl, T. (2010), "The application of modal filters for damage detection", *Smart Struct. Syst.*, **6**(2) 115-133.
- Mendrok, K., Wojcicki, J. and Uhl, T. (2015), "An application of operational detection shapes and spatial filtration for damage detection", *Smart Struct. Syst.*, **16**(6) 1049-1068.
- Nechak, L., Raynaud, H. F., Kulcsár, C. and Conan, J. M. (2014), "Mirrors' dynamics: a plague for adaptive optics systems performance?", *European Control Conference (ECC)*, Strasbourg, June.
- Noll, R.J. (1976), "Zernike polynomials and atmospheric turbulence", *J. Opt. Soc. Am.*, **66**(3) 207-211.
- Piefort, V. (2001), "Finite element modeling of piezoelectric active structures", Ph.D. dissertation, Université Libre de Bruxelles, Brussels, Belgium.
- Preumont, A. (2018), *Vibration control of active structures, an introduction*, (4th Ed.), Springer International Publishing, Switzerland.
- Roddier, F. (1999), *Adaptive optics in astronomy*, Cambridge University Press, Cambridge, UK.
- Rodrigues, G., Bastaits, R., Roose, S., Stockman, Y., Gebhardt, S., Schönecker, A., Villon, P. and Preumont, A. (2009), "Modular bimorph mirrors for adaptive optics", *Opt. Eng.*, **48**(3) 034001:1-034001:7.
- Rodrigues, G. (2010), "Adaptive Optics with Segmented Deformable Bimorph Mirrors", Ph.D. dissertation, Université Libre de Bruxelles, Brussels, Belgium.
- Tyson, R.K. (2000), *Introduction to adaptive optics*, SPIE Press, Bellingham, Washington, USA.
- Wang, K., Alaluf, D., Mokrani, B. and Preumont, A. (2017), "Dynamic control of deformable mirrors for adaptive optics", *Proceedings of the ECCOMAS Thematic Conference on Smart Structures and Materials*, Madrid, June.
- Zenz, G., Berger, W., Gerstmayr, J., Nader, M. and Krommer, M. (2013), "Design of piezoelectric transducer arrays for passive and active modal control of thin plates", *Smart Struct. Syst.*, **12**(5) 547-577.

Appendix: Zernike modes

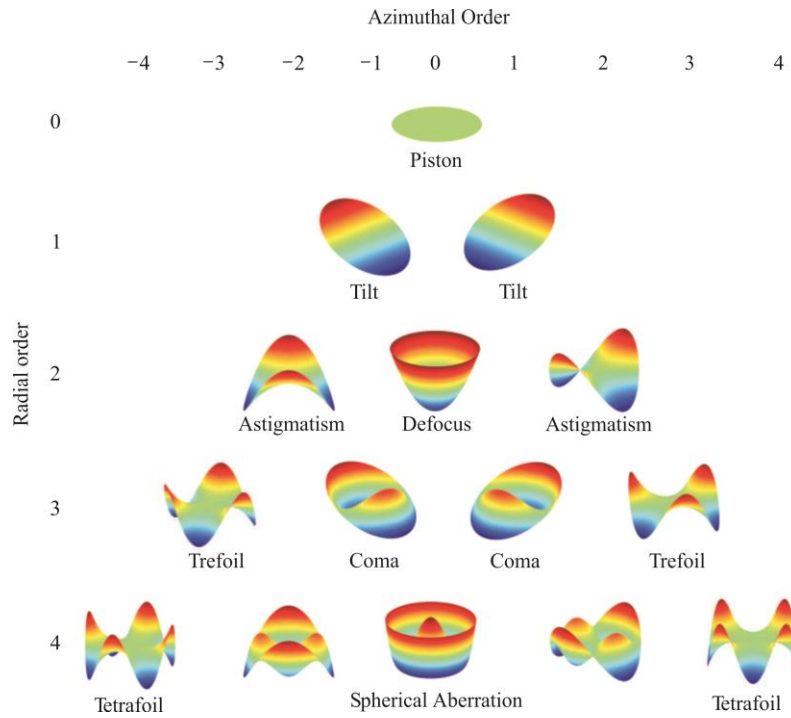


Fig. 23 Optical aberrations: low order Zernike polynomials ranked according to their azimuthal and radial order

Table 2 Zernike polynomials ($\rho < 1$)

Polynomial	Denomination
1	Piston
$2\rho \cos \theta$	Tilt
$2\rho \sin \theta$	Tilt
$\sqrt{3}(2\rho^2-1)$	Defocus
$\sqrt{6}(\rho^2 \sin 2\theta)$	Primary Astigmatism
$\sqrt{6}(\rho^2 \cos 2\theta)$	Primary Astigmatism
$\sqrt{8}(3\rho^3-2\rho) \sin \theta$	Primary Coma
$\sqrt{8}(3\rho^3-2\rho) \cos \theta$	Primary Coma
$\sqrt{8}\rho^3 \sin 3\theta$	Trefoil
$\sqrt{8}\rho^3 \cos 3\theta$	Trefoil
$\sqrt{5}(6\rho^4-6\rho^2+1)$	Spherical aberration